Report No.
UCB/SEMM-2014/06

Structural Engineering
Mechanics and Materials

Hybrid Simulation Theory for Continuous Beams

By

Paul L. Drazin, Sanjay Govindjee, and Khalid M. Mosalam

June 2014

**Department of Civil and Environmental Engineering
University of California, Berkeley**

HYBRID SIMULATION THEORY FOR CONTINUOUS BEAMS

Paul L. Drazin[1],
Sanjay Govindjee[2],
and Khalid M. Mosalam[2]

ABSTRACT

Hybrid Simulation is an experimental technique involving the integration of a physical system and a computational system with the use of actuators and sensors. This method has a long history in the experimental community and has been used for nearly 40 years. However, there is a distinct lack of theoretical research on the performance of this method. Hybrid simulation experiments are performed with the implicit assumption of an accurate result as long as sensor and actuator errors are minimized. However, no theoretical results confirm this intuition nor is it understood how minimal the error should be and what the essential controlling factors are. To address this deficit in knowledge, we consider the problem as one of tracking the trajectory of a dynamical system in a suitably defined configuration space. In order to make progress, we further consider a strictly theoretical hybrid system. This allows for precise definitions of errors during a hybrid simulation. As a model system we look at an elastic beam as well as a viscoelastic beam. In both cases we consider systems with a continuous distribution of mass as occurs in real physical systems. Errors in the system are then tracked during harmonic excitation using space-time L^2-norms defined over the system's configuration space. We then present a parametric study of how magnitude and phase errors in the control system relate to the performance of a hybrid simulation. We are able to show sharp sensitivities to control system errors. Further, we are able to show the existence of unacceptably high errors whenever excitations exceed the system's first fundamental frequency.

Keywords: hybrid system; real-time hybrid simulation; elastic beam theory; error analysis; experimental error; viscoelastic beam

BACKGROUND

Hybrid simulation is an experimental methodology in which part of a system is tested physically and the remaining part of the system is modeled computationally. The two types of substructures are then interfaced. This allows for only part of the system to be constructed and tested in order for the whole system to be

[1]Grad. Student, Dept. of Mechanical Engineering, College of Engineering, Univ. of California, Berkeley, Berkeley, CA 94720

[2]Prof., Dept. of Civil and Environmental Engineering, College of Engineering, Univ. of California, Berkeley, Berkeley, CA 94720

studied. The methodology allows for an economical means for the testing of large systems subjected to dynamical loads; see e.g. Takanashi et al. 1975, Mahin and Williams 1980, Mosalam et al. 1998. This is clearly useful for systems that are typically too large or expensive to be fully tested and for those that contain subsystems whose nonlinearities possess no known models. Hybrid simulation may be categorized into two broad types: real-time hybrid simulation and pseudo-dynamic testing or simply hybrid simulation; see e.g. Schellenberg 2008. The former uses a laboratory system to drive the experiment in a real-time setting, typically with the use of a shaking table and other actuators which provide true dynamic loads. The latter uses a step-by-step imposition of the load where the physical system moves quasi-statically and the mass and viscous damping characteristics of the system are modeled numerically. Hybrid simulation has been mainly used as a testing method in structural mechanics, especially for earthquake response testing; see e.g. Takanashi and Nakashima 1987. However, hybrid simulation is not exclusive to earthquake engineering and is widely applicable to situations where it is impractical to build a complete physical system for testing; see e.g. Bursi et al. 2011.

In order to perform hybrid testing one must of course have knowledge of the governing equations for the part of the system to be modeled in the computer; see e.g. Mosalam and Günay 2014. With this basic information, a simulation methodology must be chosen and the computer interfaced to the physical part of the system via a collection of sensors and actuators. It is noted that the sensors in the physical part of the system provide information to the computational part of the system regarding their current state and the actuators manipulate the physical part of the system based on the current state of the computational part of the system. At its essence hybrid simulation involves the splitting of a system into two parts with the assumption that the interfacing methodology allows one to accurately replicate the response of the system should one have decided to physically test it in its entirety.

Most of the work on hybrid simulation has been devoted to the actual execution of experiments; as this is large task in and of itself, little theoretical work has been performed to verify the results that these experiments produce. There has been some study of the errors associated with hybrid simulation, but in many of those situations, the errors studied were due to the entire experimental setup and numerical integration, rather than the errors directly associated with a hybrid system itself; see e.g. Shing and Mahin 1987. This paper, on the other hand, focuses solely on the *theoretical* performance of real-time hybrid simulation as an experimental method. This approach eliminates the errors associated with time integration methods and focuses only on the errors that are generated by splitting the system into a hybrid one. To make our analysis concrete, we focus on a harmonically driven simply supported beam. This system has been chosen for its relative simplicity and the ability to analyze the solution in an analytical form. We look at both the elastic as well as the viscoelastic cases. Further, we always consider the case of distributed mass as occurs in real physical objects.

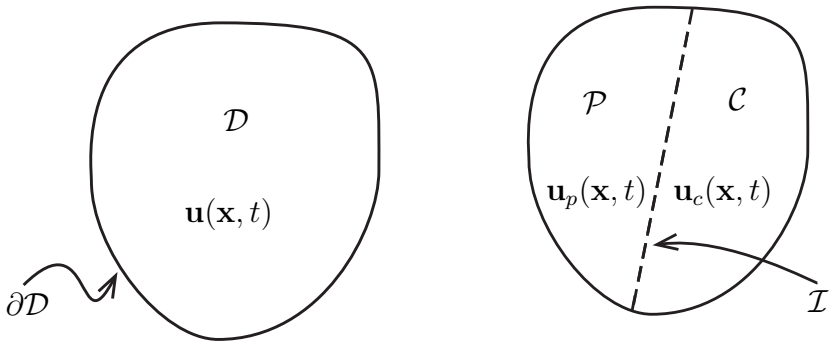

FIG. 1: (a) A general system with domain $\mathcal{D}$ and displacement $\mathbf{u}(\mathbf{x},t)$. (b) A general system with imposed separation into two substructures for comparison to the hybrid system. $\mathcal{P} \cup \mathcal{C} = \mathcal{D}$ and $\partial\mathcal{P} \cap \partial\mathcal{C} = \mathcal{I}$.

By studying the problem from a strictly theoretical viewpoint, we can fully control the situation and precisely define what we mean by *truth*. This allows us to precisely identify a lower bound below which one can not improve a hybrid simulation via, say, improvements in time integration methods. While our set up is rather simple, the results are felt to have general applicability. In what follows, we first describe the general theoretical setting of hybrid simulation; we then consider the elastic beam within this setting followed by the viscoelastic beam. This is followed by a study of the behavior of hybrid simulation for these two systems and finally a set of concluding observations and comments are presented.

GENERAL THEORY OF HYBRID SIMULATION

The Reference System

Consider a mechanical system with domain $\mathcal{D}$ as seen in Fig. 1a. In this section, the system in question is kept as general as possible to allow for further generalizations. The motion of the system is characterized by the displacement

$$\mathbf{u}(\mathbf{x},t) \text{ for } \mathbf{x} \in \mathcal{D}. \tag{1}$$

For comparison to the hybrid system, we also imagine it as separated into two or more substructures. For simplicity, this paper focuses only on two substructures for the hybrid system, a "physical" substructure ($\mathcal{P}$-side) and a "computational" substructure ($\mathcal{C}$-side) as shown in Fig. 1b, where $\mathcal{P} \cup \mathcal{C} = \mathcal{D}$ and $\partial\mathcal{P} \cap \partial\mathcal{C} = \mathcal{I}$. This allows for the displacement to be decomposed into two parts:

$$\mathbf{u}(\mathbf{x},t) = \begin{cases} \mathbf{u}_p(\mathbf{x},t) & \text{if } \mathbf{x} \in \mathcal{P} \\ \mathbf{u}_c(\mathbf{x},t) & \text{if } \mathbf{x} \in \mathcal{C}. \end{cases} \tag{2}$$

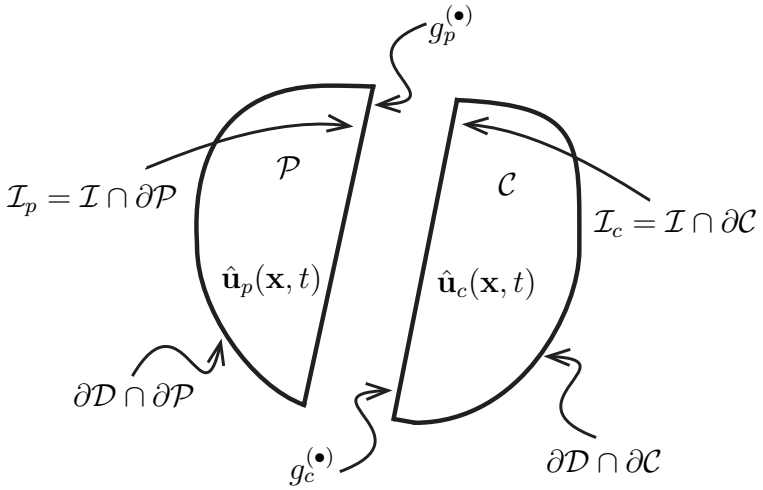

FIG. 2: The hybrid system separated into the physical, $\mathcal{P}$, and computational, $\mathcal{C}$, substructures with boundary functions $g_p^{(\bullet)}$ and $g_c^{(\bullet)}$.

This characterization represents the true response, against which a hybrid system simulation should be compared. The precise expression for $\mathbf{u}(\mathbf{x}, t)$ is found by determining the function that satisfies the governing equations of motion on $\mathcal{D}$ and the imposed boundary conditions on $\partial\mathcal{D}$.

The Hybrid System

The response of a hybrid system can be defined in a similar fashion. Using the same boundary defined in Fig. 1b, the hybrid system is separated into two substructures. In order to differentiate the reference system from the hybrid system a superposed hat ($\hat{\bullet}$) is used to indicate a quantity in the hybrid system. Thus, the displacement for the hybrid system is given as

$$\hat{\mathbf{u}}(\mathbf{x}, t) = \begin{cases} \hat{\mathbf{u}}_p(\mathbf{x}, t) & \text{if } \mathbf{x} \in \mathcal{P} \\ \hat{\mathbf{u}}_c(\mathbf{x}, t) & \text{if } \mathbf{x} \in \mathcal{C}. \end{cases} \tag{3}$$

In a hybrid system $\hat{\mathbf{u}}_p$ and $\hat{\mathbf{u}}_c$ are determined from the "solution" of the governing equations of motion for $\mathcal{P}$ and $\mathcal{C}$ subjected to the boundary conditions on $\partial\mathcal{P}$ and $\partial\mathcal{C}$. The boundary conditions on $\partial\mathcal{D} \cap \partial\mathcal{P}$ and $\partial\mathcal{D} \cap \partial\mathcal{C}$ naturally match those of the reference system. However, in the hybrid system one must additionally deal with boundary conditions on the two interface sides of $\mathcal{I}_p$ and $\mathcal{I}_c$, where $\mathcal{I}_p = \mathcal{I} \cap \partial\mathcal{P}$ and $\mathcal{I}_c = \mathcal{I} \cap \partial\mathcal{C}$. The conditions on $\mathcal{I}_p$ and $\mathcal{I}_c$ are provided by the sensor and actuator system. Here we model these by boundary functions $g_p^{(\bullet)}$ and $g_c^{(\bullet)}$ as shown in Fig. 2. The number of boundary functions needed is determined by the hybrid system so that the system is mathematically determinate. Since the boundary functions take on the role of boundary conditions, for every boundary function on the $\mathcal{P}$-side, there is a corresponding boundary function on the $\mathcal{C}$-side. The boundary functions take into consideration the imperfection of the dynamics of the hybrid system, such as time-delays between the two sides, as

well as the magnitude of tracking errors in the motion and traction as needed by the system at hand. In the analysis, we formulate the correspondence between related boundary functions by the relation

$$\underline{D}[\hat{\mathbf{u}}_c]\Big|_{\mathcal{I}_c} = \underline{E}\ \underline{D}[\hat{\mathbf{u}}_p]\Big|_{\mathcal{I}_p}, \tag{4}$$

where $\underline{D}[\bullet]$ is an operator that generates the necessary boundary functions at the interface from the displacements $\hat{\mathbf{u}}_{(\bullet)}$ and $\underline{E}$ is an error operator that applies different error parameters to the different boundary functions created by $\underline{D}[\bullet]$. Later in this paper, we employ a simple magnitude and phase error model for $\underline{E}$. This allows us to study the effects of a wide variety of hybrid system errors. These types of errors are chosen due to their direct correlation to experimental systems; see e.g. Shing and Mahin 1987 or Ahmadizadeh et al. 2008.

L^2 Space and Hybrid Simulation Error

With the above notation in hand, let us consider in further detail how one can understand hybrid simulation from a *geometric* point of view. Let us first define the L^2 function space as (see e.g. Johnson 2009):

$$L^2(\Omega) = \{\mathbf{v} : \mathbf{v} \text{ is defined on } \Omega \text{ and } \int_\Omega \mathbf{v}^2 \mathrm{d}\mathbf{x} < \infty\}, \tag{5}$$

where Ω is a bounded domain in $\mathbb{R}^3$. Using this definition we have

$$\mathbf{u} \in L^2(\mathcal{D}). \tag{6}$$

The restriction of $\mathbf{u}$ onto $\mathcal{C}$ is denoted as

$$\mathbf{u}_c \in L^2(\mathcal{C}) \tag{7}$$

and similarly for the restriction of $\mathbf{u}$ onto $\mathcal{P}$:

$$\mathbf{u}_p \in L^2(\mathcal{P}). \tag{8}$$

The same applies for the $(\hat{\bullet})$ quantities. We note that

$$L^2(\mathcal{D}) = L^2(\mathcal{C}) \times L^2(\mathcal{P}). \tag{9}$$

In $L^2(\mathcal{C})$, the displacements $\mathbf{u}_c$ and $\hat{\mathbf{u}}_c$ trace out trajectories with time. These two trajectories differ from each other since they are for two different systems. The same is true for the trajectories of $\mathbf{u}_p$ and $\hat{\mathbf{u}}_p$ in $L^2(\mathcal{P})$. By considering the trajectories in $L^2(\mathcal{C})$ and $L^2(\mathcal{P})$ as components of order pairs in $L^2(\mathcal{D})$ at each moment in time, we can combine trajectories from $L^2(\mathcal{C})$ and $L^2(\mathcal{P})$ into trajectories in $L^2(\mathcal{D})$, one for the reference system and one for hybrid system. A simple illustration of this situation is shown in Fig. 3. The difference between the two trajectories in $L^2(\mathcal{D})$ gives us the basis for our error analysis. Given a true

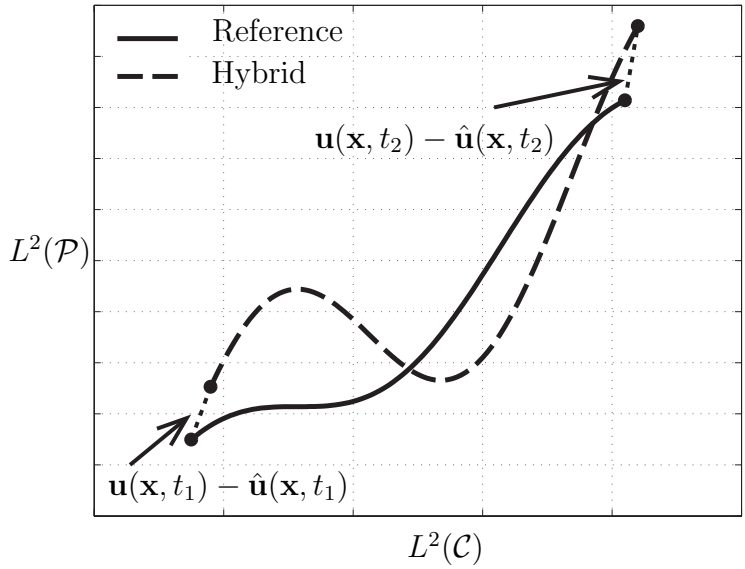

FIG. 3: A schematic illustration of a possible $L^2(\mathcal{D})$ space with trajectories for the reference and hybrid systems from time $t = t_1$ to time $t = t_2$ showing the difference between the two trajectories.

solution $\mathbf{u}$ and a hybrid solution $\hat{\mathbf{u}}$, we measure error using a space-time L^2-norm in the form of (10); see e.g. Johnson 2009:

$$||e|| = \left(\int_0^T \int_{\mathcal{D}} \left| \mathbf{u}(\mathbf{x}, t) - \hat{\mathbf{u}}(\mathbf{x}, t) \right|^2 d\mathbf{x} dt \right)^{1/2}, \tag{10}$$

where T is the period of the harmonic excitation on the system and $\mathcal{D}$ is the complete domain of the system. This allows for a measurement of the absolute error between the reference system and the hybrid system over the domain of the mechanical system and over the period of the harmonic excitation.

APPLICATION TO THE ELASTIC BEAM

The foregoing set-up is now applied to a continuous beam, where we have access to exact analytical solutions for an intact reference system and for a hybrid (decomposed) system defined over $\mathcal{P}$ and $\mathcal{C}$.

Reference System

Our reference system is an elastic, homogeneous beam pinned on both ends with a harmonic moment applied to one end. A diagram of the mechanical system is shown in Fig. 4. In this case the displacement can be decomposed as shown in (11):

$$\mathbf{w} = w(x, t)\mathbf{e}_z, \tag{11}$$

where $\mathbf{e}_z$ represents the unit vector in the z-direction as indicated in Fig. 4. In what follows, the vector form is ignored, and only $w(x, t)$ is considered. The

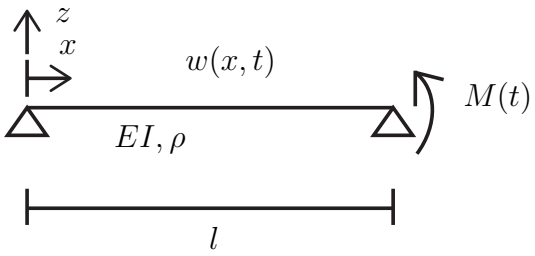

FIG. 4: The system of an elastic pinned-pinned beam with applied moment, $M(t)$.

partial differential equation that governs the motion of the mechanical system is given by the dynamic form of the classical Bernoulli-Euler equation:

$$\rho\ddot{w} = -EIw_{,xxxx}, \tag{12}$$

where ρ is the linear mass density, E is the elastic modulus, I is the second moment of area of the beam, and comma notation indicates differentiation. The applied moment, M, is described by

$$M(t) = \bar{M}\exp(i\omega t), \tag{13}$$

where $\bar{M}$ is the magnitude of the applied moment and ω is the frequency of the applied moment. The well-known solution to this system is given by

$$w(x,t) = \left(\frac{-\bar{M}\sin(\beta x)}{2EI\beta^2\sin(\beta l)} + \frac{\bar{M}\sinh(\beta x)}{2EI\beta^2\sinh(\beta l)}\right)\exp(i\omega t), \tag{14}$$

where l is the beam span and the parameter β is determined from

$$\beta^4 = \frac{\rho}{EI}\omega^2. \tag{15}$$

Hybrid System

The pinned-pinned beam is now represented by a hybrid system using a specific separation. The hybrid system is shown in Fig. 5, where the $\mathcal{P}$-side is the left side, without the applied moment, and the $\mathcal{C}$-side is the right side, with the applied moment. The separation of the hybrid system occurs at $x = l_1$; thus, in this system, the displacement is given by

$$\hat{w}(x,t) = \begin{cases} \hat{w}_p(x,t) & \text{if } 0 \le x < l_1 \\ \hat{w}_c(x,t) & \text{if } l_1 < x \le l. \end{cases} \tag{16}$$

Separation of variables is applied to the system, giving $\hat{w}_p(x,t) = \hat{X}_p(x)\hat{T}_p(t)$ and $\hat{w}_c(x,t) = \hat{X}_c(x)\hat{T}_c(t)$, where both must independently satisfy (12). This leads to the following equations:

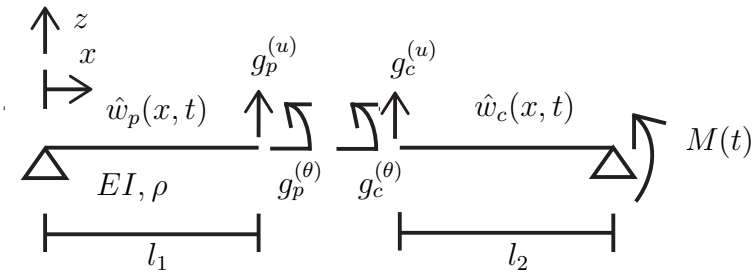

FIG. 5: The hybrid system of an elastic pinned-pinned beam with applied moment, $M(t)$, and boundary functions $g_p^{(u)}(t)$, $g_c^{(u)}(t)$, $g_p^{(\theta)}(t)$, and $g_c^{(\theta)}(t)$, $l_1+l_2=l$.

$$\hat{X}_p(x) = \hat{b}_1\cos(\hat{\beta}_p x) + \hat{b}_2\sin(\hat{\beta}_p x) + \hat{b}_3\cosh(\hat{\beta}_p x) + \hat{b}_4\sinh(\hat{\beta}_p x), \tag{17a}$$

$$\hat{X}_c(x) = \hat{b}_5\cos(\hat{\beta}_c x) + \hat{b}_6\sin(\hat{\beta}_c x) + \hat{b}_7\cosh(\hat{\beta}_c x) + \hat{b}_8\sinh(\hat{\beta}_c x), \tag{17b}$$

$$\hat{T}_p(t) = \hat{T}_c(t) = \exp(i\omega t), \tag{17c}$$

where $\hat{b}_1 - \hat{b}_8$ are constants. Since $\hat{w}_p$ and $\hat{w}_c$ must both independently satisfy (12), the following relation also holds:

$$\hat{\beta}_p^4 = \hat{\beta}_c^4 = \frac{\rho}{EI}\omega^2. \tag{18}$$

Using (18) in conjunction with (15), it is noted that $\beta = \hat{\beta}_p = \hat{\beta}_c$. In order to determine $\hat{b}_1 - \hat{b}_4$, we will need four boundary conditions on $\mathcal{P}$. As is typical, we will take two from the left-side and two from the right-side of the domain $\mathcal{P}$. Following the convention defined previously, $g_p^{(\bullet)}$ will denote the boundary functions on $\mathcal{I}_p$, which in the present case is simply the point $x = l_1$. The same applies for $\hat{b}_5 - \hat{b}_8$ on $\mathcal{C}$ where the boundary functions on $\mathcal{I}_c$ will be denoted by $g_c^{(\bullet)}$. As an example, Fig. 5 shows boundary functions $g_p^{(u)}$ and $g_c^{(u)}$ for transverse displacements and $g_p^{(\theta)}$ and $g_c^{(\theta)}$ for rotations. Thus, the boundary conditions at $x = l_1$ become

$$\hat{w}_p(l_1,t) = g_p^{(u)}(t) = \bar{g}_p^{(u)}\exp(i\omega t), \tag{19a}$$

$$\hat{w}_c(l_1,t) = g_c^{(u)}(t) = \bar{g}_c^{(u)}\exp(i\omega t), \tag{19b}$$

$$\hat{w}_{p,x}(l_1,t) = g_p^{(\theta)}(t) = \bar{g}_c^{(\theta)}\exp(i\omega t), \tag{19c}$$

$$\hat{w}_{c,x}(l_1,t) = g_c^{(\theta)}(t) = \bar{g}_c^{(\theta)}\exp(i\omega t). \tag{19d}$$

Note that $\bar{g}_p^{(\bullet)}$ and $\bar{g}_c^{(\bullet)}$ are so far unspecified. Intuitively they are related to each other but we will defer a discussion of this inter-relation to when we discuss a model for the interface errors.

Solving for $\hat{b}_1 - \hat{b}_8$, while employing the requisite boundary conditions at $x = 0$, $x = l$, $\mathcal{I}_p$, and $\mathcal{I}_c$, gives

$$\hat{w}_p(x,t) = \frac{\bar{g}_p^{(u)} D_2(\beta l_1, \beta x) - \frac{\bar{g}_p^{(\theta)}}{\beta} D_3(\beta l_1, \beta x)}{D_2(\beta l_1, \beta l_1)} \exp(i\omega t), \tag{20}$$

$$\hat{w}_c(x,t) = \left(\frac{\bar{M}}{2EI\beta^2} \Big(A_1(\beta l_2) B_1\left(\beta(x - l_1)\right) - B_1(\beta l_2) A_1\left(\beta(x - l_1)\right) \Big) \right.$$
$$\left. - \bar{g}_c^{(u)} D_2(\beta l_2, \beta(x - l)) + \frac{\bar{g}_c^{(\theta)}}{\beta} D_3(\beta(x - l), \beta l_2) \right) \frac{\exp(i\omega t)}{D_2(\beta l_2, \beta l_2)}, \tag{21}$$

where

$$A_1(x) = \sin(x) - \sinh(x), \tag{22a}$$
$$B_1(x) = \cosh(x) - \cos(x), \tag{22b}$$
$$D_2(x,y) = \cosh(x)\sin(y) - \cos(x)\sinh(y), \tag{22c}$$
$$D_3(x,y) = \sinh(x)\sin(y) - \sin(x)\sinh(y). \tag{22d}$$

Non-Dimensionalization and Determination of $\bar{g}_p^{(\bullet)}$ and $\bar{g}_c^{(\bullet)}$

To further the analysis, one needs to determine the so far unspecified boundary functions. In this regard, it is advantageous to non-dimensionalize the equations as well as to express the reference solution in the same format as the hybrid solution. For the latter point, an examination of (14) and (22) shows that one can write the reference solution as

$$w(x,t) = \frac{\bar{M} D_3(\beta x, \beta l)}{2EI\beta^2 P_1(\beta l)} \exp(i\omega t), \tag{23}$$

where

$$P_1(x) = \sin(x)\sinh(x). \tag{24}$$

In order to non-dimensionalize (20), (21), and (23), we introduce the following non-dimensional quantities:

$$\eta = \frac{w}{l}, \quad \hat{\eta}_p = \frac{\hat{w}_p}{l}, \quad \hat{\eta}_c = \frac{\hat{w}_c}{l}, \quad y = \frac{x}{l}, \tag{25a}$$

$$\mu = \frac{\bar{M} l}{EI}, \tag{25b}$$

$$\omega_1 = \sqrt{\frac{EI}{\rho}} \frac{\pi^2}{l^2}, \quad \Omega = \frac{\omega}{\omega_1}, \quad \tau = \omega_1 t, \tag{25c}$$

$$\kappa = \beta l = \pi\sqrt{\Omega}, \tag{25d}$$

$$G_p^{(u)} = \frac{\bar{g}_p^{(u)}}{l}, \quad G_c^{(u)} = \frac{\bar{g}_c^{(u)}}{l}, \quad G_p^{(\theta)} = \bar{g}_p^{(\theta)}, \quad G_c^{(\theta)} = \bar{g}_c^{(\theta)}, \tag{25e}$$

$$L_1 = \frac{l_1}{l}, \quad L_2 = 1 - L_1, \tag{25f}$$

where ω_1 is the lowest resonant frequency of the pinned-pinned beam; see e.g. Tongue 2002. Thus (20), (21), and (23) become

$$\eta(y,\tau) = \frac{\mu D_3(\kappa y,\kappa)}{2\kappa^2 P_1(\kappa)} \exp(i\Omega\tau), \tag{26}$$

$$\hat{\eta}_p(y,\tau) = \frac{G_p^{(u)} D_2(\kappa L_1,\kappa y) - \frac{G_p^{(\theta)}}{\kappa} D_3(\kappa L_1,\kappa y)}{D_2(\kappa L_1,\kappa L_1)} \exp(i\Omega\tau), \tag{27}$$

$$\begin{aligned}\hat{\eta}_c(y,\tau) = \Bigg(&\frac{\mu}{2\kappa^2}\Big(A_1(\kappa L_2)B_1(\kappa(y-L_1)) - B_1(\kappa L_2)A_1(\kappa(y-L_1))\Big) \\ &- G_c^{(u)} D_2(\kappa L_2,\kappa(y-1)) + \frac{G_c^{(\theta)}}{\kappa} D_3(\kappa(y-1),\kappa L_2)\Bigg) \frac{\exp(i\Omega\tau)}{D_2(\kappa L_2,\kappa L_2)}.\end{aligned} \tag{28}$$

For the rest of this section, unless stated otherwise, all new variables or quantities are assumed to be dimensionless.

To complete the system of equations, $G_p^{(\bullet)}$ and $G_c^{(\bullet)}$ need to be determined. The conditions to determine $G_P^{(\bullet)}$ and $G_c^{(\bullet)}$ come from the characteristics of the sensor and actuator control system. As a simple model, we assume that the hybrid system produces a magnitude and phase error in the corresponding displacements, rotations, bending moments, and shear forces across the interface of the hybrid system. Using the notation introduced in (4), we write $\underline{D}[\bullet]$ as

$$\underline{D}[\bullet] = \begin{bmatrix} \bullet \\ \frac{\partial \bullet}{\partial y} \\ \frac{\partial^2 \bullet}{\partial y^2} \\ \frac{\partial^3 \bullet}{\partial y^3} \end{bmatrix}, \tag{29}$$

and express $\underline{E}$ as a 4×4 matrix with $(1+\epsilon_{(\bullet)})\exp(i\Omega d_{(\bullet)})$ on the diagonal and zeros everywhere else. Here, $\epsilon_{(\bullet)}$ are the magnitude of the tracking errors for the displacement, rotation, bending moment, and shear force at the interface and $d_{(\bullet)}$ are the tracking error time delays of the displacement, rotation, bending moment, and shear force. $\epsilon_{(\bullet)}$ and $d_{(\bullet)}$ model the interface error in the hybrid system at $\mathcal{I}$. Using this model gives

$$\hat{\eta}_c(L_1,\tau) = \hat{\eta}_p(L_1,\tau)(1+\epsilon_u)\exp(i\Omega d_u), \tag{30a}$$

$$\hat{\eta}_{c,y}(L_1,\tau) = \hat{\eta}_{p,y}(L_1,\tau)(1+\epsilon_\theta)\exp(i\Omega d_\theta), \tag{30b}$$

$$\hat{\eta}_{c,yy}(L_1,\tau) = \hat{\eta}_{p,yy}(L_1,\tau)(1+\epsilon_M)\exp(i\Omega d_M), \tag{30c}$$

$$\hat{\eta}_{c,yyy}(L_1,\tau) = \hat{\eta}_{p,yyy}(L_1,\tau)(1+\epsilon_V)\exp(i\Omega d_V). \tag{30d}$$

Equations (30) can be used to analytically solve for $G_p^{(\bullet)}$ and $G_c^{(\bullet)}$ and thus complete the solution; see Drazin 2013. Note that this error model can be made more sophisticated but suffices to understand a number of features of hybrid systems.

APPLICATION TO THE VISCOELASTIC BEAM

The same pinned-pinned beam model used previously is adopted for the viscoelastic case. For this purpose we introduce the complex elastic modulus:

$$E^* = E' + iE'', \tag{31}$$

where E' is the storage modulus, E'' is the loss modulus, and $i = \sqrt{-1}$ is the imaginary unit; see e.g. Ferry 1970. To be concrete, we will employ the standard 3-parameter Maxwell model for a linear viscoelastic solid (the so-called standard linear solid); see e.g. Tschoegl 1989. In this case,

$$E' = E_\infty + \frac{\omega^2 t_r^2}{1+\omega^2 t_r^2}(E_0 - E_\infty), \tag{32a}$$

$$E'' = \frac{\omega t_r}{1+\omega^2 t_r^2}(E_0 - E_\infty), \tag{32b}$$

where E_0 is the instantaneous modulus and E_∞ is the equilibrium modulus. The relaxation time, t_r, is given by

$$t_r = \frac{1}{\omega_1 \zeta}. \tag{33}$$

The parameter ζ is the non-dimensional damping frequency, which determines the location of the damping peak in the frequency domain. Since E^* is complex, it can be expressed in polar form by

$$E^* = |E^*|\exp(i\delta), \tag{34a}$$

$$|E^*| = \sqrt{E'^2 + E''^2}, \tag{34b}$$

$$\delta = \tan^{-1}\left(\frac{E''}{E'}\right). \tag{34c}$$

Using this form of the complex elastic modulus, (15) becomes

$$\rho\omega^2 = |E^*| I \exp(i\delta)\beta^4. \tag{35}$$

Since ω, $|E^*|$, I, and ρ are real values, β must be complex. Solving for β results in

$$\beta = \sqrt[4]{\frac{\rho}{|E^*|I}}\sqrt{\omega}\exp\left(\frac{-i\delta}{4}\right). \tag{36}$$

The solution for the reference system now reads

$$w(x,t) = \left(\frac{-\bar{M}\exp(-i\delta)\sin(\beta x)}{2|E^*|I\beta^2\sin(\beta l)} + \frac{\bar{M}\exp(-i\delta)\sinh(\beta x)}{2|E^*|I\beta^2\sinh(\beta l)}\right)\exp(i\omega t). \tag{37}$$

The non-dimensionalization of (37) and the application of the functions defined by (22) and (24) lead to the same relation given by (26), where all values have the same definitions as before except

$$\kappa = \beta l = \pi\sqrt{\Omega}\exp\left(\frac{-i\delta}{4}\right), \tag{38a}$$

and

$$\mu = \frac{\bar{M} l \exp(-i\delta)}{|E^*|I}. \tag{38b}$$

Likewise, (27) and (28) hold for the viscoelastic pinned-pinned hybrid beam case, using the new definitions of κ and μ.

ANALYSIS OF THE HYBRID SYSTEMS

Having analytic expressions for the response of the reference systems and the hybrid systems, we are now in a position to examine the intrinsic errors associated with hybrid simulation using our interface model. Error in hybrid simulation for a given loading and a given set of $\epsilon_{(\bullet)}$ and $d_{(\bullet)}$ will be defined using the non-dimensionalized response functions as

$$e(y,\tau) = \eta(y,\tau) - \hat{\eta}(y,\tau). \tag{39}$$

For analysis purposes we will examine the L^2-norm of this quantity defined by

$$||e_p||^2 = \int_0^T \int_0^{L_1} \Big(\mathrm{Re}\big(\eta(y,\tau) - \hat{\eta}_p(y,\tau)\big)\Big)^2 dy d\tau, \tag{40a}$$

$$||e_c||^2 = \int_0^T \int_{L_1}^{1} \Big(\mathrm{Re}\big(\eta(y,\tau) - \hat{\eta}_c(y,\tau)\big)\Big)^2 dy d\tau, \tag{40b}$$

$$||e|| = \sqrt{||e_p||^2 + ||e_c||^2}, \tag{40c}$$

where T is the non-dimensional period of the applied bending moment, meaning that it changes with Ω and $\mathrm{Re}(\bullet)$ is the real part of $(\bullet)$. The functions $\eta(y,\tau)$, $\hat{\eta}_p(y,\tau)$, and $\hat{\eta}_c(y,\tau)$ are from (26), (27), and (28), respectively. Due to the complexity of developing an analytic form for these norms, we choose to numerically evaluate the integrals appearing in the norm expressions with a high order adaptive quadrature rule to at least an absolute error of 10^{-10} and at least a relative error of 10^{-6}.

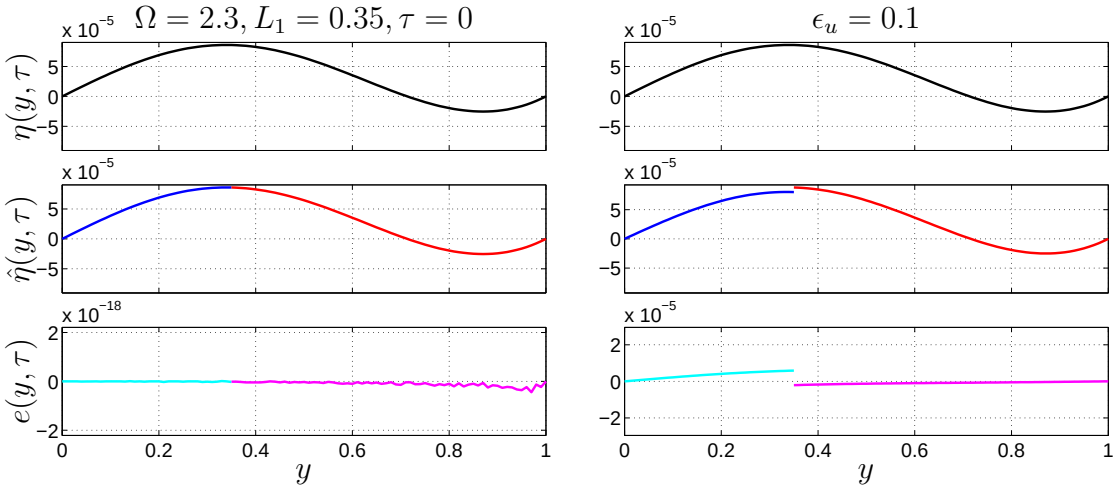

FIG. 6: (a) Comparison of the reference elastic pinned-pinned beam to the hybrid elastic pinned-pinned beam with zero interface errors. (b) Comparison of the reference elastic pinned-pinned beam to the hybrid elastic pinned-pinned beam when $\epsilon_u = 0.1$. Note, $\mu = 3.75 \times 10^{-3}$.

Analysis of the Elastic Beam

First, (27) and (28) are compared with (26) to verify that the equations do in fact describe the correct system. Note that if all $\epsilon_{(\bullet)} = 0$ and $d_{(\bullet)} = 0$, then the hybrid system should reduce to the reference system. Figure 6a shows $\eta(y,0)$ and $\hat{\eta}(y,0)$ for one set of parameters and the difference $e(y,0)$. Note that $e(y,0)$ is zero to machine precision and thus, to the accuracy to which we can evaluate the expressions, they are identical. For all of the following figures, all error parameters are assumed to be 0 unless noted otherwise in the figure and μ is taken as 3.75×10^{-3}. To show the effects of a displacement error, a 10% error is introduced into the displacement by setting $\epsilon_u = 0.1$. Fig. 6b shows a discontinuity between the two sides of the interface in the hybrid system and that a noticeable amount of error has been introduced into the entire domain of the hybrid system due to this 10% displacement error at the interface; the large difference in scale of the vertical axes of the error plots in Figs. 6a and 6b should be noted.

Effect of Varying Frequency

For specific choices of the parameters $\epsilon_{(\bullet)}$, $d_{(\bullet)}$, and L_1, Ω is initially swept from 10^{-2} to 10^2 to give a comprehensive look at the effect of the excitation frequency on the hybrid system. Note, that all $\epsilon_{(\bullet)}$ have similar effects on the error, and thus only ϵ_u is discussed, with any differences explicitly stated for the other $\epsilon_{(\bullet)}$. The same holds for $d_{(\bullet)}$. In Fig. 7a, which has $\epsilon_u = 0.1$, the error grows extremely large near the resonant frequencies of the system, i.e. $\Omega = 1, 4, 9, ...$, which is

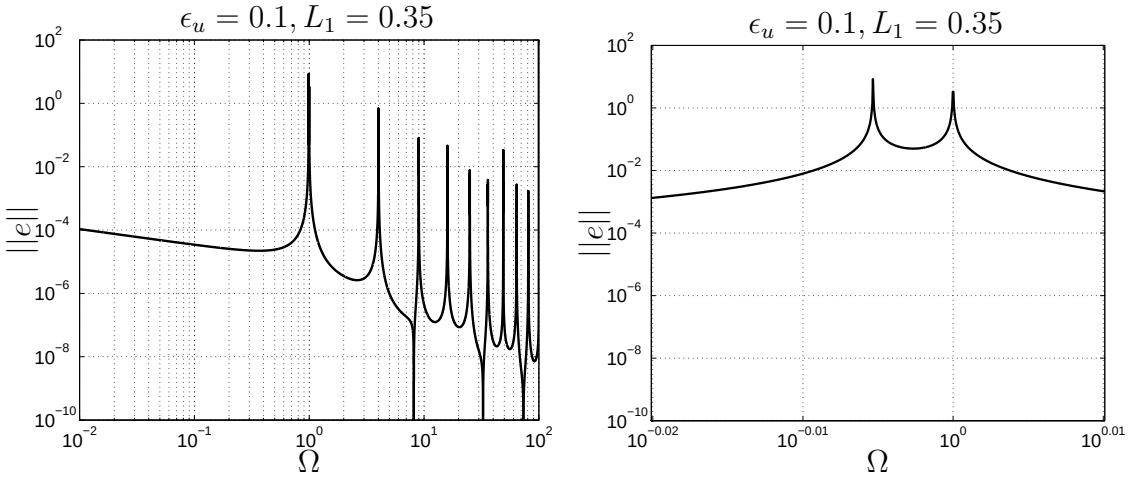

FIG. 7: Error norms. (a) A frequency sweep of the elastic pinned-pinned beam with $\epsilon_u = 0.1$ on a log-log plot. (b) A zoomed in plot showing the parasitic spike just to the left of $\Omega = 1$.

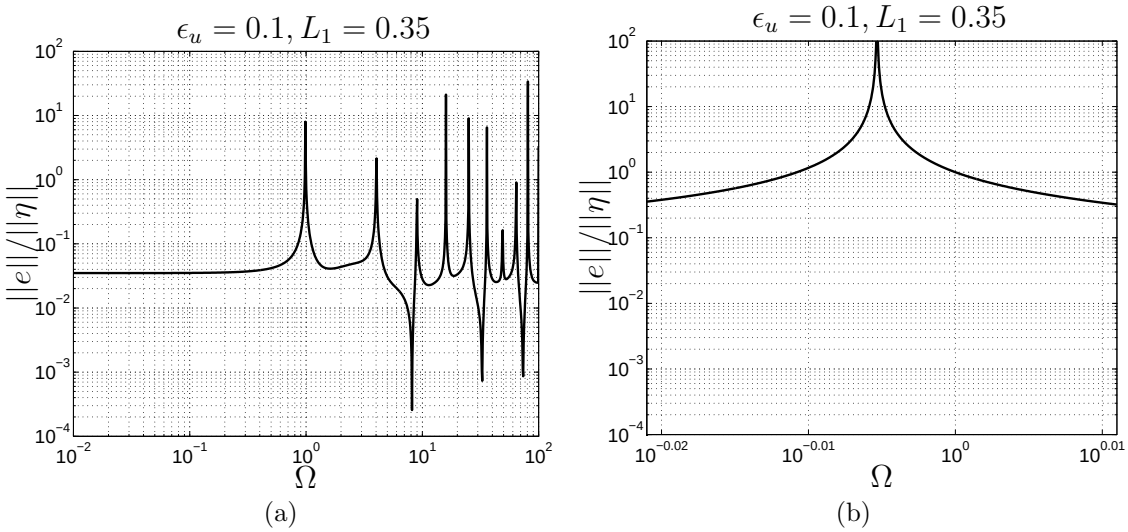

FIG. 8: Normalized error norms. (a) A frequency sweep of the elastic pinned-pinned beam with $\epsilon_u = 0.1$ on a log-log plot. (b) A zoomed in plot showing the parasitic spike just to the left of $\Omega = 1$.

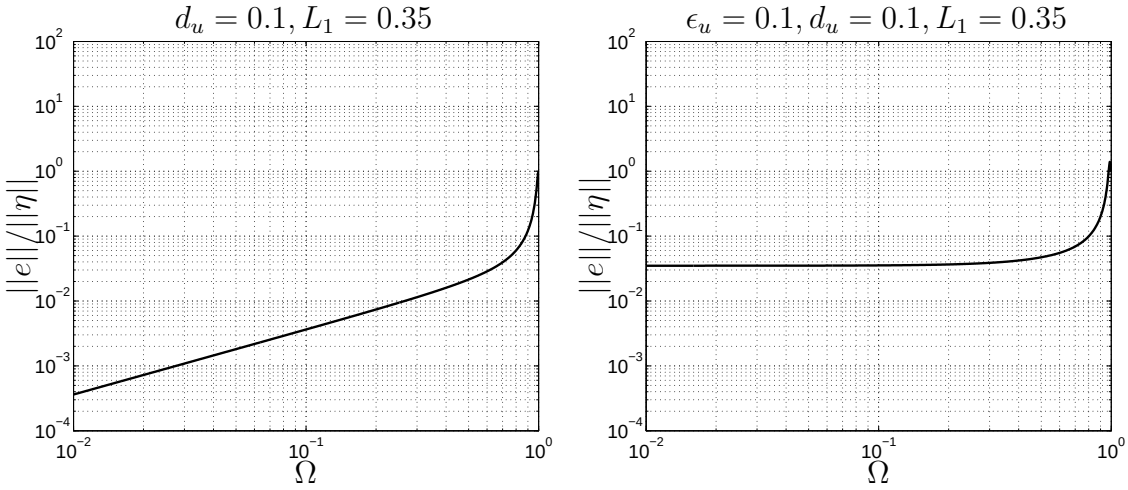

FIG. 9: (a) A frequency sweep of the elastic pinned-pinned beam with $d_u = 0.1$ on a log-log plot. (b) A frequency sweep of the elastic pinned-pinned beam with $\epsilon_u = 0.1$ and $d_u = 0.1$ on a log-log plot.

to be expected as the displacement becomes unbounded at these frequencies. Since almost all types of excitation contain a broad spectrum of frequencies, this leads us to conclude that in order for the hybrid system to give usable results all frequencies in the excitation must be less than the first resonant frequency, or $\Omega = 1$. Because of this, in what follows our analysis will focus on excitation frequencies that are below the first resonant frequency ($\Omega < 1$). An important feature of the hybrid system response is the appearance of parasitic resonant spikes not associated with the actual resonant frequencies of the reference system. Figure 7b shows one such spike just to the left of $\Omega = 1$. These parasitic spikes are more noticeable for different values of the system parameters. The parasitic spikes oscillate around the resonant frequencies as L_1 changes from zero to one. The amplitudes of these oscillations, in the frequency domain, are directly related to the values of $\epsilon_{(\bullet)}$. It is also helpful to plot the error norm normalized by $||\eta||$ to give a sense of the relative magnitude of the error. For the same parameters as considered in Fig. 7, this is shown in Fig. 8. Comparing Figs. 8a and 7a, one notes that the drop off in error with increasing frequency disappears. This is due to the fact that $||\eta||$ is inversely proportional to $\sqrt{\Omega}$. While the error spikes seem similar in the two cases, an examination of the zoomed in normalized error in Fig. 8b, cf. Fig. 7b, shows that the hybrid system somewhat tracks the reference system at $\Omega = 1$ but that it clearly possesses a true parasitic resonance just below $\Omega = 1$.

Considering now the effect of time delay errors, Fig. 9a shows the case of $d_u = 0.1$; the normalized error is now seen to grow for increasing frequencies below $\Omega = 1$. This is in contrast to what is seen in Fig. 8a, where the normalized

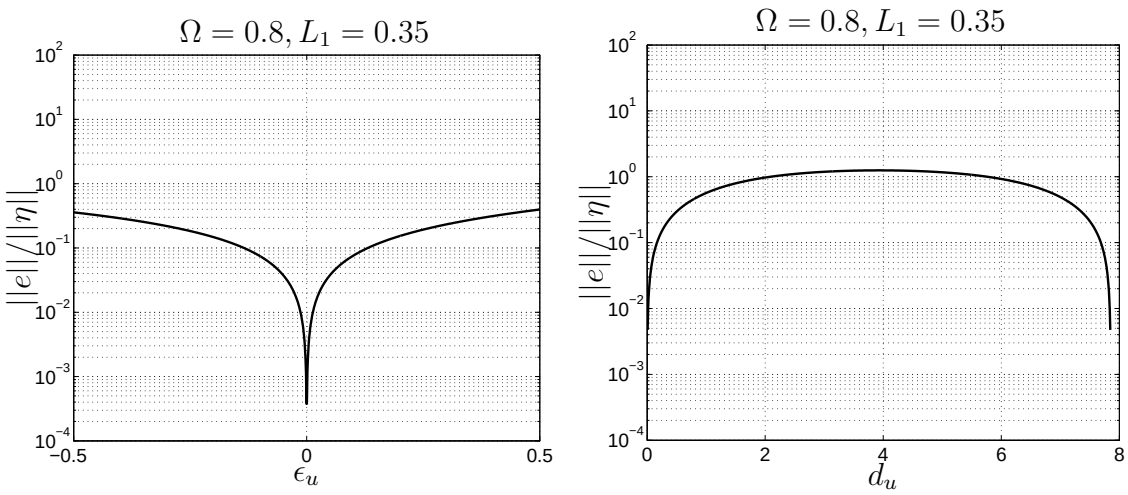

(a) (b)

FIG. 10: (a) The effect of varying ϵ_u for the elastic beam with no other imposed error on a linear-log plot. (b) The effect of varying d_u for the elastic beam with no other imposed error on a linear-log plot.

error held constant with increasing frequency until it approached the first resonant frequency. Further, with the presence of multiple error sources, the behavior is modestly additive. Consider for example non-zero ϵ_u and d_u as shown in Fig. 9b. In this instance the normalized error, prior to $\Omega = 1$, behaves exactly as in Fig. 8a. This indicates that with multiple non-zero error parameters, the error in the hybrid system will be controlled by the largest individual error for equivalent values of the error parameters.

Effect of Varying $\epsilon_\mathbf{u}$*: Magnitude of Tracking Error*

The effect of varying ϵ_u is studied to determine its direct effect on the hybrid system error. As an example, in Fig. 10a, we show the effect of varying ϵ_u at $\Omega = 0.8$. The domain of ϵ_u only extends from -0.5 to 0.5, since it is highly unlikely that an experimental setup will have tracking errors outside of this domain. It can be seen that as ϵ_u increases in magnitude, the rate of normalized error change decreases. Thus, the only areas of large change in the error come from locations near $\epsilon_u = 0$. This indicates that there is noticeable error in the hybrid system, even for small ϵ_u, and trying to reduce the value of ϵ_u does not have a large effect on the system error, unless ϵ_u can be brought quite close to zero. Note that varying ϵ_θ, ϵ_M, and ϵ_V produces similar results to those in Fig. 10a.

Effect of Varying $\mathbf{d_u}$*: Phase of Tracking Error*

The effect of varying d_u is analyzed to determine its direct effect on the error in the hybrid system. Since the effects of d_u are periodic, d_u is varied from 0 to $2\pi/\Omega$. For Ω, we again choose a value of 0.8 for illustrative purposes. As shown in Fig. 10b, the normalized error grows from zero, peaks when d_u is half of the

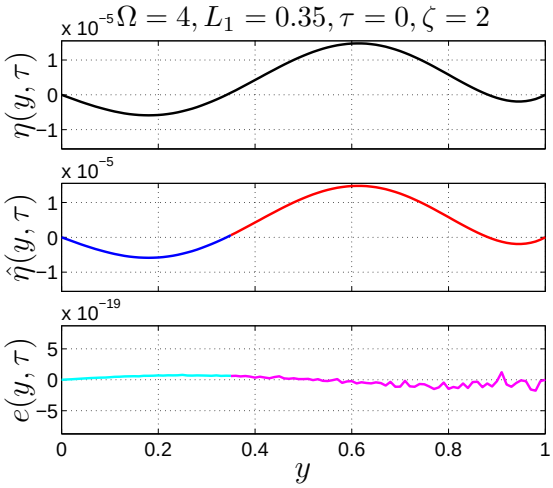

FIG. 11: Comparison of the reference viscoelastic pinned-pinned beam to the hybrid viscoelastic pinned-pinned beam with no imposed error.

period, and then falls when d_u is equal to a period. Note that varying d_θ, d_M, and d_V produces similar results as in Fig. 10b.

Analysis of the Viscoelastic Beam

We now turn our attention to the viscoelastic beam. As viscoelasticity introduces damping it provides a somewhat more realistic model system. As an initial check of our basic relations, equations (27) and (28) with $\epsilon_{(\bullet)} = d_{(\bullet)} = 0$ are compared with the equation for the solution to the reference viscoelastic beam, (26). This comparison is shown in Fig. 11. For succinctness, only the real part of the solution is shown. As it can be seen, only round-off error is present between the hybrid and reference systems. It should be noted that the applied frequency chosen was $\Omega = 4$, which is a resonant frequency of the elastic system, meaning that the displacement is unbounded in the equivalent elastic case. However in Fig. 11, the displacement is bounded due to viscoelastic damping. Note that $\zeta = 2$ implies that the damping peak is located at a frequency of 2. If ζ was chosen to be farther from the applied frequency, the effects of the damping would be significantly less.

Effect of Varying Frequency

As with the elastic beam, a sweep of the frequency is performed from $\Omega = 10^{-2}$ to $\Omega = 10^2$ for various values of ζ with $\mu_0 = \bar{M}l/E_0I = 3.75 \times 10^{-3}$ and $\mu_\infty = \bar{M}l/E_\infty I = 2\mu_0$. It is noted that the effects of all magnitude errors $\epsilon_{(\bullet)}$ are nearly identical and thus only ϵ_u is considered. This is the same for all time delay errors $d_{(\bullet)}$. Consider first the effect of a magnitude error ϵ_u as shown in Fig. 12a. We note that, depending on the value of ζ, the error is bounded to differing degrees at all of the resonant frequencies of the elastic case. In what follows, we will focus on frequencies less than 10 ($\Omega < 10$). Similar to the elastic beam case, there are parasitic resonant spikes near the resonant frequencies, but only when the

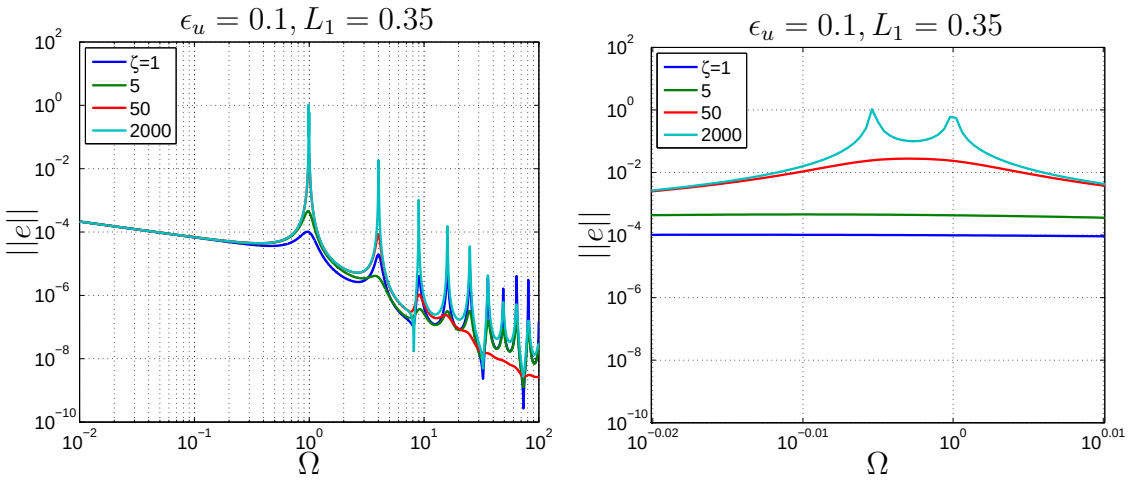

FIG. 12: Error norms: (a) A frequency sweep of the viscoelastic pinned-pinned beam with $\epsilon_u = 0.1$ on a log-log plot for various values of ζ. (b) A zoomed in plot of the parasitic resonant spike to the left of $\Omega = 1$.

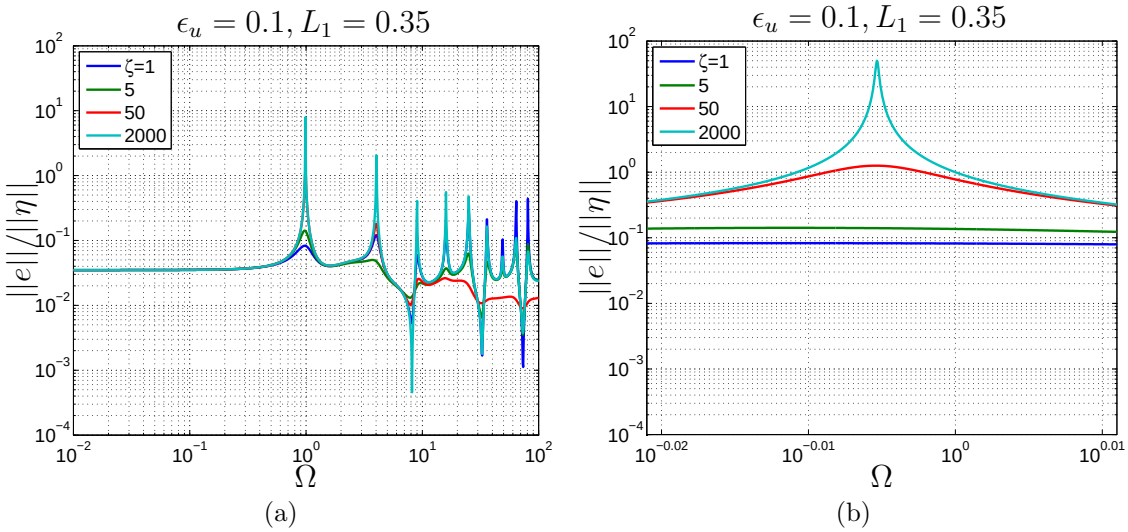

FIG. 13: Normalized error norms: (a) A frequency sweep of the viscoelastic pinned-pinned beam with $\epsilon_u = 0.1$ on a log-log plot for various values of ζ. (b) A zoomed in plot of the parasitic resonant spike to the left of $\Omega = 1$.

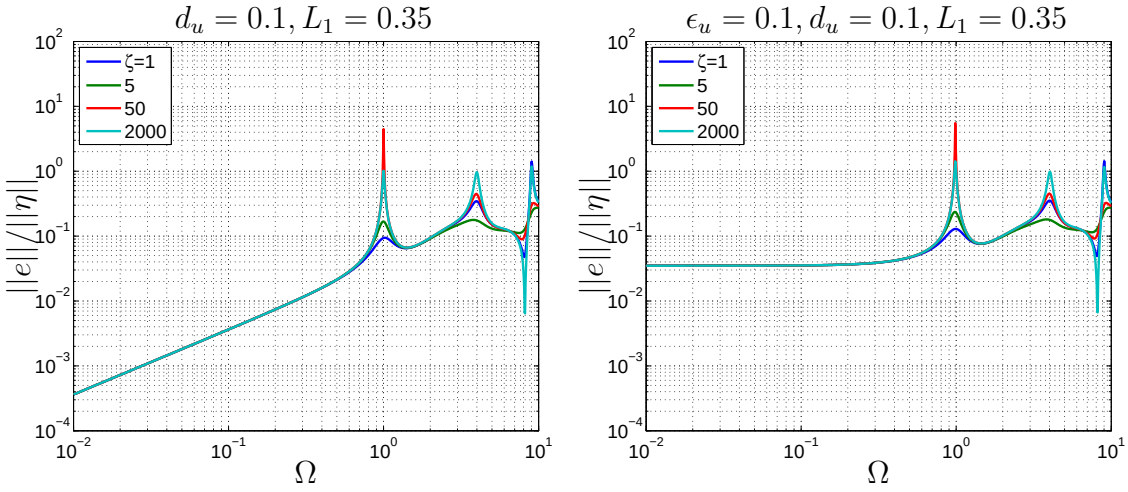

FIG. 14: (a) A frequency sweep of the viscoelastic pinned-pinned beam with $d_u = 0.1$ on a log-log plot with varying ζ. (b) A frequency sweep of the viscoelastic pinned-pinned beam with $\epsilon_u = 0.1$ and $d_u = 0.1$ on a log-log plot with varying ζ.

drive frequency is far from the damping frequency; one of these parasitic spikes is shown in Fig. 12b, but only for the $\zeta = 2000$ curve. In the other three curves, any possible parasitic spikes are mollified by the viscoelastic damping. When present, these parasitic spikes oscillate around the resonant frequency peaks as L_1 grows from zero to one and the amplitude of these oscillations are related to the value of $\epsilon_{(\bullet)}$ just as in the elastic case. As before, normalized error plots are helpful for interpreting the results as shown in Fig. 13. The general interpretations from the elastic case are seen also to hold here with the caveat that the placement of damping peaks near (elastic) resonances will reduce errors. If we instead introduce phase error, d_u (see Fig. 14a), we observe behavior similar to the elastic case – again with the same caveat. When the applied frequency is near the damping frequency, the error is reduced around the resonant frequencies. When the applied frequency is far from the damping frequency, the error curves resemble those of the elastic case. Also, similar to the elastic case below $\Omega = 1$, the error behaves the same as in Figs. 8a and 9a.

In order to determine how the error parameters interact in the viscoelastic case, two error parameters are applied to the hybrid system. Figure 14b has $\epsilon_u = 0.1$ and $d_u = 0.1$. Below $\Omega = 1$, the normalized error is seen to be consistent with Fig. 13a and not with Fig. 14a. This indicates that the larger error of the individual error parameters controls the error of the system with multiple non-zero error parameters, which is consistent with the elastic beam case. Further inspection of Figs. 12a and 14 reveals a sharp drop in the error to the left of $\Omega = 10$. This drop in error occurs when $\sin(\kappa L_1) = 0$. In fact for non-zero ϵ_u, ϵ_M, d_u, and d_M error drops occur whenever $\sin(\kappa L_1) = 0$. For non-zero ϵ_θ, ϵ_V, d_θ,

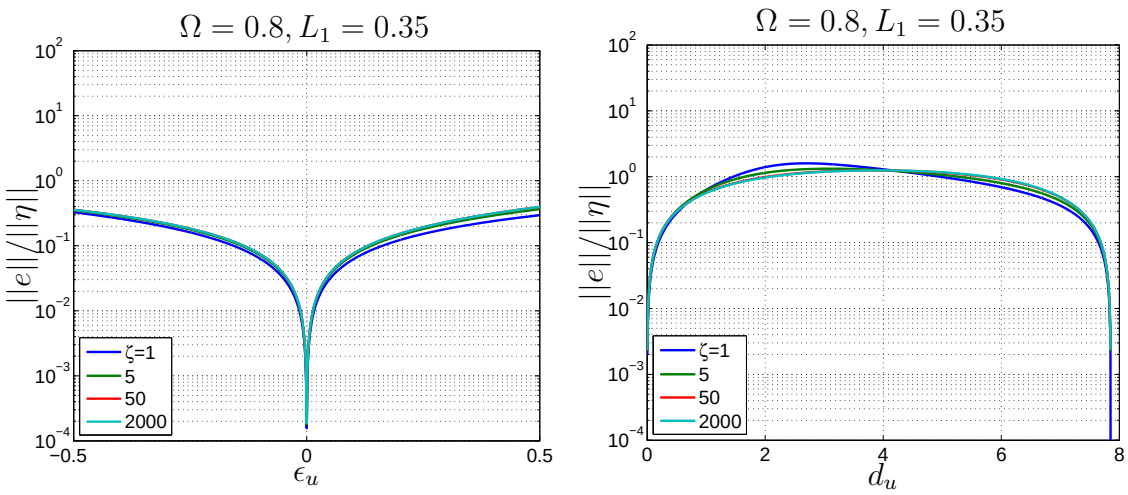

(a) (b)

FIG. 15: (a) The effect of varying ϵ_u for the viscoelastic beam with no other imposed error on a linear-log plot. (b) The effect of varying d_u for the viscoelastic beam with no other imposed error on a linear-log plot.

and d_V such error drops occur whenever $\cos(\kappa L_1) = 0$. These observations also hold for the elastic case but are largely irrelevant there since in the elastic case one should never exceed $\Omega = 1$.

Effect of Varying $\epsilon_\mathbf{u}$*: Magnitude of Tracking Error*

To understand the effect of varying ϵ_u in the viscoelastic case, we consider the fixed frequency $\Omega = 0.8$ at multiple values for ζ within the range -0.5 to 0.5. As shown in Fig. 15a, the shape of the error curves are identical to the ones in Fig. 10a. However, the curve for $\zeta = 1$ is ever so slightly below the rest of the curves due to the fact that the damping frequency is close to the excitation frequency. Also, as in the elastic case, the error changes rapidly for small ϵ_u and levels off as ϵ_u grows in magnitude. The effect of varying ϵ_θ, ϵ_M, and ϵ_V are similar and thus not shown.

Effect of Varying $\mathbf{d_u}$*: Phase of Tracking Error*

The effect of varying d_u in the viscoelastic case is shown in Fig. 15b. As noted earlier, the effects of d_u are periodic over the range 0 to $2\pi/\Omega$. As a concrete example, Fig. 15b shows the case of $\Omega = 0.8$. When the applied frequency is far from the damping frequency, the curves behave similar to that of the elastic case, cf. Fig. 10b. However when the damping frequency is closer to the applied frequency, the error, while remaining essentially the same, develops a slight asymmetry relative to the center of the range as seen with the curves for $\zeta = 1$ and $\zeta = 5$. Varying d_θ, d_M, and d_V produces similar results.

Note that in the viscoelastic case, when the applied frequency is far from the damping frequency, the error curves behave in the same manner as the elastic

case. This is to be expected, because away from the damping frequency, the viscoelastic equations approach the elastic ones. Finally, note that almost all conclusions gained from the elastic case are repeated for the viscoelastic case, except for special treatment of the parameter ζ.

CONCLUSION

The analysis in this paper demonstrates the theoretical performance of hybrid simulation of an elastic and a viscoelastic beam for the special case where the only errors that are present are those associated with the hybrid (i.e. split system) nature of the formulation. A harmonic excitation was applied and only the steady-state solution was studied. This ignores any transient response that may occur in experimental implementations of hybrid simulation. The results show that the resonant frequencies have an outsized impact on the error of the simulation system. Thus, in order for real-time hybrid simulation to be effective as a simulation technique, one must be aware of the forcing frequencies, and keep them below the first resonant frequency for the elastic case or possibly near the damping frequency in the viscoelastic case. The error due to $\epsilon_{(\bullet)}$ grows quickly around $\epsilon_{(\bullet)} = 0$ and reaches a large error value for small $\epsilon_{(\bullet)}$ values. Thus, it is somewhat impractical to reduce the $\epsilon_{(\bullet)}$ parameters in order to reduce the error in the system, because unless one can make the $\epsilon_{(\bullet)}$ values quite small, the system error does not significantly change. All of the results stated in the analysis section have also been corroborated with hybrid formulations for an elastic and a viscoelastic axially loaded bar (see Drazin 2013) as well as for a classical elastic Kirchhoff-Love plate; see Bakhaty et al. 2014. This indicates that there are universal errors that occur in hybrid simulation, even for simple one-dimensional and two-dimensional problems. Awareness of the causes of these errors can allow for real-time hybrid simulations to be conducted in a way that reduces or even prevents these errors.

In this paper it was assumed that $\epsilon_{(\bullet)}$ and $d_{(\bullet)}$ are constants. However, this is not always the case, they may in fact be functions of the frequency, such that at higher frequencies the time-delay or magnitude error may increase. To include this effect, one could introduce models of the form

$$d_{(\bullet)} = \frac{d_0}{\Big(1 + \exp(\Omega_0 - \Omega)\Big)^2}, \tag{41}$$

where d_0 is the maximum time delay and Ω_0 is the frequency of maximum growth rate; see Bakhaty et al. 2014. Similar equations can be applied to $\epsilon_{(\bullet)}$. Such models modify the details of the error responses; however, the trends remain fundamentally the same.

This paper considered a single homogeneous linear material that could be modeled by (12). This is not always the case for an experimental setup of hybrid simulation. For example, many hybrid simulation setups are for many bars and beams at the same time, each interacting with the whole system; see e.g. Mosalam

and Günay 2014 or Günay and Mosalam 2014. In such cases analytic response solutions are likely to not be available but we do not expect the observed general trends to be altered.

The error measure we focused on was the L^2-norm of the displacement error but that only shows one part of error in the system. The error in the rotation, shear force, and bending moment can also be studied with the use of Sobolev-seminorms of the displacement field; see e.g. Johnson 2009. Understanding the error in these quantities is as important as understanding the error in the displacement because in some situations these quantities can be of equal or even greater importance to the structural and mechanical behavior of a system than the displacement; see e.g. Elkhoraibi and Mosalam 2007.

ACKNOWLEDGEMENTS

This research was financially supported by National Science Foundation Award Number CMMI-1153665. Any opinions, findings, and conclusions or recommendations expressed are those of the authors and do not necessarily reflect those of the National Science Foundation.

REFERENCES

Ahmadizadeh, M., Mosqueda, G., and Reinhorn, A. M. (2008). "Compensation of actuator delay and dynamics for real time hybrid structural simulation." *Earthquake Engineering and Structural Dynamics*, 37, 21–42.

Bakhaty, A. A., Govindjee, S., and Mosalam, K. M. (2014). "Theoretical development of hybrid simulation applied to plate structures." *Report No. UCB-PEER-2014-02*, Pacific Earthquake Engineering Research Center, Berkeley, CA.

Bursi, O. S., Jia, C., Vulcan, L., Neild, S. A., and Wagg, D. J. (2011). "Rosenbrock-based algorithms and subcycling strategies for real-time nonlinear substructure testing." *Earthquake Engineering and Structural Dynamics*, 40, 1–19.

Drazin, P. L. (2013). "Hybrid Simulation Theory Featuring Bars and Beams." M.S. report, University of California, Berkeley, CA. URL: http://www.ce.berkeley.edu/∼sanjay/DrazinPaulMSReportFall2013.pdf.

Elkhoraibi, T. and Mosalam, K. M. (2007). "Towards error-free hybrid simulation using mixed variables." *Earthquake Engineering and Structural Dynamics*, 36, 1497–1522.

Ferry, J. D. (1970). *Viscoelastic Properties of Polymers*. John Wiley & Sons, New York.

Günay, S. and Mosalam, K. M. (2014). "Seismic performance evaluation of high voltage disconnect switches using real-time hybrid simulation: II. parametric study." *Earthquake Engineering and Structural Dynamics*, 43, 1223–1237.

Johnson, C. (2009). *Numerical Solution of Partial Differential Equations by the Finite Element Method*. Dover Publications, Mineola, NY.

Mahin, S. A. and Williams, M. E. (1980). "Computer controlled seismic performance testing." *Dynamic Response of Structures: Experimentation, Observation, Prediction and Control*, American Society of Civil Engineers.

Mosalam, K. M. and Günay, S. (2014). "Seismic performance evaluation of high voltage disconnect switches using real-time hybrid simulation: I. system development and validation." *Earthquake Engineering and Structural Dynamics*, 43, 1205–1222.

Mosalam, K. M., White, R. N., and Ayala, G. (1998). "Response of infilled frames using pseudo-dynamic experimentation." *Earthquake Engineering and Structural Dynamics*, 27, 589–608.

Schellenberg, A. H. (2008). "Advanced implementation of hybrid simulation." Ph.D. thesis, University of California, Berkeley, CA.

Shing, P. S. B. and Mahin, S. A. (1987). "Elimination of spurious higher-mode response in pseudodynamic tests." *Earthquake Engineering and Structural Dynamics*, 15, 409–424.

Takanashi, K. and Nakashima, M. (1987). "Japanese activities on on-line testing." *Journal of Engineering Mechanics*, 113, 1014–1032.

Takanashi, K., Udagawa, K., Seki, M., Oakada, T., and Tanaka, H. (1975). "Nonlinear earthquake response analysis of structures by a computer-actuator on-line system." *Bulletin of Earthquake Resistant Structure Research Center*, 8.

Tongue, B. H. (2002). *Principles of Vibration*. Oxford University Press, New York.

Tschoegl, N. W. (1989). *The Phenomenological Theory of Linear Viscoelastic Behavior*. Springer-Verlag, Berlin.